Modeling of short-pulse laser-metal interactions in the warm dense matter regime using the two-temperature model

G. M. Petrov, A. Davidson, D. Gordon, and J. Peñano

Phys. Rev. E **103**, 033204 — Published 23 March 2021

DOI: 10.1103/PhysRevE.103.033204

Modeling of short pulse laser-metal interactions in the Warm Dense Matter regime using the two-temperature model

G. M. Petrov, A. Davidson*, D. Gordon, and J. Peñano
Naval Research Laboratory, Plasma Physics Division, 4555 Overlook Ave. SW, Washington, DC 20375, USA
* National Research Council Research Associate, Naval Research Laboratory
02 08-2021

Abstract

A numerical model for laser-matter interactions in the Warm Dense Matter regime is presented with broad applications, e.g. ablation, thermionic emission and radiation. A novel approach is adopted, in which a complete set of collisional and transport data is calculated using a quantum model and incorporated into the classical two-temperature model for the electron and lattice/ion temperatures. The data set was produced by the Average Atom Model that combines speed, conceptual simplicity and straightforward numerical development. Such data are suitable for use in the Warm Dense Matter regime, where most of the laser-matter interactions at moderate intensities occur, thus eliminating deficiencies of previous models, e.g. interpolation between solid and ideal plasma regimes. In contrast to other works, we use a more rigorous definition of *solid* and *plasma* states of the metal, based on the physical condition of the lattice, crystalline (ordered) versus melted (disordered), rather than a definition based on electron temperature. The synergy between the two-temperature and Average Atom models has been demonstrated on a problem involving heating and melting of the interior of Al by a short pulse laser with duration 0.1−1 ps and laser fluences 1×10^3–3×10^4 J/m^2 (0.1-3 J/cm^2). The melting line, which separates the solid and plasma regimes, has been tracked in time and space. The maximum melting depth has been determined as function of laser fluence: $l_{melt}(\mu m) \cong 4\times10^3 F(\frac{J}{m^2})$.

1. Introduction

Interaction of short-pulse lasers with metals at moderate laser fluence (~TW/cm^2) generates, beneath and above the surface, a non-ideal plasma that is typically in the Warm Dense Matter (WDM) regime. It is characterized with electron density comparable to the solid density and electron temperature of a few eV. Many phenomena are associated with such plasmas, most notably ablation [1,2,3,4], thermionic emission [5,6] and bremsstrahlung radiation [7]. The laser energy absorption and energy transfer to the lattice are often modeled using the two-temperature model (Ref. [8,9,10,11,12], to name a few), which treats the electrons and ions as two separate sub-systems governed by the equations

$$\frac{\partial}{\partial t}(\bar{C}_e n_e k_b T_e) = \frac{\partial}{\partial z}\left(k_e \frac{\partial T_e}{\partial z}\right) - G(T_e - T_i) + P \tag{1a}$$

$$(\bar{C}_i + \Delta\bar{H}_m \delta(T_i - T_m)) n_i k_b \frac{\partial T_i}{\partial t} = \frac{\partial}{\partial z}\left(k_i \frac{\partial T_i}{\partial z}\right) + G(T_e - T_i) \tag{1b}$$

where k_B is the Boltzmann constant, T_α is the temperature, n_α is the density, $\bar{C}_\alpha = C_\alpha/(k_b n_\alpha)$ is the normalized heat capacity and k_α is the thermal conductivity of species α=*e*,*i*. The parameter G is the rate of energy transfer from electrons to ions and P is the local power absorption per unit volume from the laser field (to be specified later). The term containing the normalized latent heat of fusion, $\Delta\bar{H}_m = \Delta H_m/R$, accounts for the solid-to-liquid transition at the melting temperature T_m [13], in which the gas constant R=8.3145 J/(mol*K) is used as a conversion factor.

Equations (1) are a sub-set of a more general (three-dimensional) set of equations. We account for parameter variation only along the laser propagation direction, *z*, and neglect transverse gradients. The latter is justified by the characteristic dimensions of the system under consideration: the transverse dimensions are comparable to the laser focal spot diameter (~1 mm), while the longitudinal dimensions are on the order of a few microns (cf. Figures 6 and 8). Equations (1) are solved to yield the spatio-temporal evolution of the electron and lattice/ion temperatures. For the purpose of illustration of the concept proposed in this paper, i.e. the synergy between a model for laser-matter interaction and another model for computing a suitable set of collisional/transport data (the Average Atom Model), our study is limited to heating and melting, providing a foothold for a wider range of processes and phenomena such as the one mentioned above.

But even in a process as "simple" as melting, we must consider the material phases characterized by the presence of a regular ion lattice structure. In the early stage of interaction ($t < 1$ ps) the lattice is still intact, while at later times ($t > 1$ ps) the lattice melts, forming dense plasma. The physical state of the metal is different during the two stages of the interaction, and so are the coefficients in Equations (1). In the former, the metal is in its *solid state*, i.e. spatially ordered crystal, and the coefficients are derived from classical solid-state physics considerations. In the latter, the lattice has collapsed to a dense mix of electrons and ions, i.e. the system is now in a liquid, or *plasma state*. Obviously, the two states must be modeled with different sets of parameters, and assumptions. For example, in the solid state the collisional and transport parameters are governed by electron-phonon interactions, while in the plasma state the interactions become electron-ion. The liquid (plasma) state can be naturally extended to vapor state, prevalent in phenomena such as surface ablation, but it is not considered in this work.

In the above, we consider thermal melting only. There are other mechanisms that may come into play. Non-thermal melting can occur due to excessive electron temperature or removal of electrons, causing the lattice to collapse, i.e. "cold ablation" (electrons pulling out ions from the lattice) [14], Coulomb explosion [13], or fast (fs-ps) energy density deposition. If pressure builds that exceeds the Young modulus, a strong shock wave emerges that compresses the material and causes structural damage [15].

Though the overall interaction dynamics is well-known, it is the distinction between the two states and definition of coefficients we are concerned with. To date, the separation has been based on "low" and "high" electron temperature with the plasma state being inevitably modeled by some variation of the Spitzer's formulas for ideal fully ionized gas. However, at solid densities the Spitzer's formulas become applicable only at large electron temperatures, in excess of 50-60 eV. Thus, the vast majority of simulations take place neither in the solid, nor in ideal plasma limit, but rather, in the intermediary Warm Dense Matter regime (Figure 1).

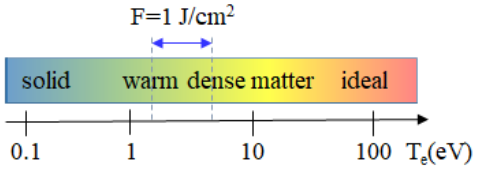

Figure 1: Illustration of the various regimes encountered or transitioned through during short pulse laser matter interactions at moderate intensities (~TW/cm^2). The Warm Dense Matter regime spans roughly from a fraction of eV to ~50 eV. The dashed lines indicate the typical maximum electron temperature range for commonly used metals (Al, Cu and Au) at laser fluence 10^4 J/m^2 (1 J/cm^2) [8,9].

In the last two decades a considerable body of work conclusively showed that the Warm Dense Matter regime is a state of matter in its own right that cannot be modeled by a simple interpolation of adjacent regimes. A single, yet compelling argument in favor of the last statement is conveyed by Fig. 2.

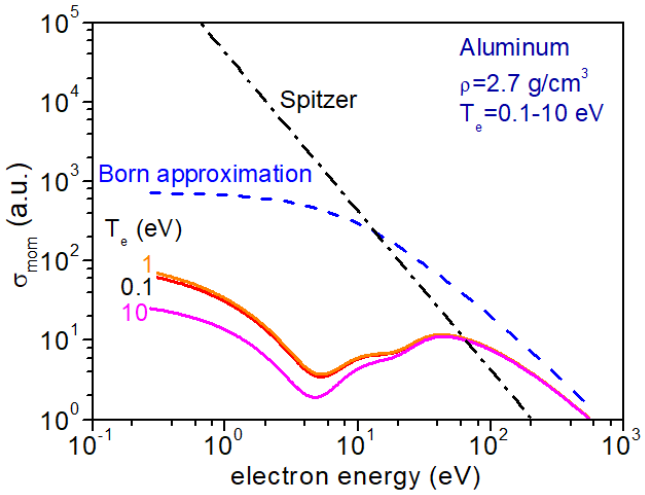

Figure 2: Electron-ion momentum-transfer cross sections in atomic units (2.8×10^{-21} m^2) calculated using the Average Atom Model for T_e=0.1, 1 and 10 eV (solid lines), the Born approximation (dashed line) and Spitzer's formula with ln(L)=2 (dashed-dot line).

The momentum-transfer cross section, which is at the heart of nearly all collisional and transport coefficients, as well as power absorption via Inverse Bremsstrahlung, is plotted in Figure 2 as calculated by the quantum model discussed in Section 2 (solid lines). The Spitzer's Coulomb cross section is orders of magnitude larger, a point recently made by Starrett [16]. The next candidate, the Born approximation, is quantum by nature and offers an improvement, but it is valid only for "weak" electron-ion interactions, i.e. high electron energies (>100 eV). At low kinetic energies (1-20 eV), in which we are primarily interested in, it lacks accuracy and is still an order of magnitude larger compared to the quantum model. Thus, neither the classical Coulomb cross section nor the cross section calculated in the Born approximation are adequate for computing collisional rates and transport parameters.

The above arguments speak strongly of the need to perform quantum-mechanical calculations to compute cross sections and related transport parameters. In addition, it is imperative to revisit the earlier distinction between solid and plasma states. In this paper, we adopt a novel approach in which (i) the two states are separated based on the *physical* condition of the lattice: crystalline (ordered) versus "melted" (disordered), which is related to the lattice temperature, rather than the electron temperature; and (ii) we calculate the coefficients in the plasma state by using a quantum model appropriate for this state, i.e. Warm Dense Matter. We dispose of the Spitzer's formulas except for the electron-electron collision rate at high temperature. The interpolation between solid and plasma states is preserved; however, in this work it is between "crystalline" and "disordered", not "high" and "low" electron temperature and the transition point (the melting temperature) is unambiguously defined. In Sections 2 we recount the coefficients in the solid state and introduce the coefficients in the plasma state, and in Section 3 we present simulation results using the two-temperature model. Section 4 discusses the Average Atom Model in context of other models, and we conclude in Section 5.

2. Collisional and transport coefficients

In the *solid state* the electron transport coefficients are well known from both published papers [1,2,8,9,10,11,12,17,18,19] and solid state physics books [20,21] and will be only briefly recalled. The electron-phonon and electron-electron collision rates are (in SI units)

$$\nu_{e-ph}(T_\ell) = k_s \frac{e_0^2}{4\pi\varepsilon_0 \hbar \mathrm{v}_F} \frac{k_B T_\ell}{\hbar} \tag{2}$$

$$\frac{1}{\nu_{ee}^2(T_e)} = \frac{1}{\nu_{solid}^2(T_e)} + \frac{1}{\nu_{Spitzer}^2(T_e)}, \tag{3}$$

respectively, where $\nu_{solid}(T_e) = k_e \frac{k_B T_e}{\varepsilon_F} \frac{k_B T_e}{\hbar}$ and $\nu_{Spitzer}(T_e) = \frac{4\sqrt{\pi}}{3}\left(\frac{e_0^2}{4\pi\varepsilon_0 m_e}\right)^2 \left(\frac{k_B T_e}{m_e}\right)^{-3/2} n_i \ln(\Lambda)$ are the rates in the solid and plasma states, respectively. In Equations (2) and (3) e_0 is the magnitude of the electron charge, ε_0 is the permittivity of free space, $\hbar$ is the reduced Plank constant, m_e is the electron mass, and $\mathrm{v}_F = \sqrt{\frac{\varepsilon_F}{2m_e}}$ and $\varepsilon_F = \frac{\hbar^2}{2m_e}(3\pi^2 n_e)^{2/3}$ are the Fermi velocity and energy, respectively. The parameter $\ln(\Lambda) = \frac{1}{2}\ln\left(1 + b_{max}^2/b_{min}^2\right)$ is the Coulomb log with $b_{min} = max\left(\frac{\hbar}{2m_e\bar{v}}, \frac{\bar{Z}e_0^2}{4\pi\varepsilon_0 m_e \bar{v}^2}\right)$ and $b_{max} = max(\lambda_{DH}, r_{WS})$ being the minimum and maximum impact parameters in which $\bar{v}$ is the electron thermal velocity, $\bar{Z}$ is the average ionization, r_{WS} is the Wigner-Seitz radius (defined later) and λ_{DH} is the Debye-Huckel screening length (for details, refer to Ref. [16]). Coefficients k_s and k_e are on the order of unity (typically between 0.1 and 10) and are specific for each element. The electron-electron collision rate, ν_{solid}, has been derived in the limit of zero temperature and is generally valid for $T_e \ll \varepsilon_F$ [22,23]. Above the Fermi energy, the collision rate levels off to a value on the order of ~10^{15} s^{-1} ([23], Fig. 1).

Since we are not aware of analytical formulas for $T_e \gg \varepsilon_F$, in order to prevent gross overestimation of the collision rate, we suggest replacing the T_e^2 in the formula for $\nu_{solid}(T_e)$ with $\max\{T_e^2, \varepsilon_F^2\}$. Note also, that the Fermi energy associated with it may change due to finite-temperature effects. To account for that, we correct the Fermi energy when the average ionization and consequently, the electron density change. The normalized electron heat capacity is an interpolation between the degenerate and ideal plasma limits given by [8,9]

$$\bar{C}_e(T_e) = \frac{3\pi^2 k_B T_e}{\sqrt{36\varepsilon_F^2 + 4\pi^4 (k_B T_e)^2}} \tag{4}$$

The electrical and thermal conductivity are taken in their standard form,

$$\sigma_{dc} = \frac{n_e e_0^2}{m_e \nu_{e-ph}} \tag{5a}$$

$$\kappa_{dc} = \frac{1}{3} C_e \frac{\mathrm{v}_F^2}{\nu_{e-ph}} \tag{5b}$$

and the electron-phonon coupling constant G is taken from the literature [24,25]. The electron-phonon rate enters the local power absorbed by the plasma, $P = \frac{e_0^2 E^2}{2m_e(\nu_{e-ph}^2 + \omega_0^2)} \nu_{e-ph} n_e$, where $E = \sqrt{\frac{2I(z,t)}{\varepsilon_0 c}}$ and ω_0 are the laser field and frequency, respectively, I is the laser intensity and c is the speed of light. The laser intensity along z is modeled as $I(z,t) = 2AI(t)\exp\left(-\frac{2z}{\ell_{skin}}\right)$ with ℓ_{skin} being the skin layer thickness and A is the absorption coefficient, to be specified later. The conventional skin depth, $\ell_{skin} = \frac{c}{\omega_p}$, where $\omega_p = \sqrt{\frac{n_0 e_0^2}{\varepsilon_0 m_e}}$ is the plasma frequency, was replaced by the collisional skin depth [26]

$$\ell_{skin} = \frac{c}{\omega_p}\left[\frac{2(1+\delta^2)}{1+(1+\delta^2)^{1/2}}\right]^{1/2}, \tag{6}$$

where the parameter $\delta = \frac{\nu_{mom}}{\omega_0}$ is the ratio of the electron collision frequency to the laser frequency.

In the *solid state* the average ion charge $\bar{Z}$ is not known and must be determined separately. In this work, it is calculated from the Average Atom Model and is used in both the solid and plasma states. The electron density is calculated according to $n_e = \bar{Z} n_i$.

Less than a picosecond after the laser pulse interacts with the metal surface, the lattice temperature reaches the melting point and the lattice collapses into a mix of electrons and ions. This is the *plasma state*. A "warm" plasma is formed with electron temperature of a few eV, putting it in the Warm Dense Matter regime. There are numerous approaches with various degree of accuracy, e.g. Density Functional Theory (DFT), Quantum Molecular Dynamics (QMD) and Path Integral Monte Carlo (PIMC), but they are computationally very intense. A reasonable trade-off is the Average Atom Model, which, albeit approximate, is fully quantum and fast (a few seconds of computation time), capable of producing large data tables for any combination of ion density and electron temperature. For this reason, all coefficients in the *plasma state* are computed with the Average Atom Model.

We now review the Average Atom Model and its building blocks, which is outlined in a number of works. [27,28,29,30,31,32,33,34,35,36]. It is a fully quantum model that falls into the category of the so-called cellular methods developed by Wigner and Seitz [37,38]. A sphere surrounding an atom is defined by the Wigner-Seitz radius $r_{WS} = \left(4\pi n_i / 3\right)^{-1/3}$ (the average distance between atoms). An ion with charge Z is placed in the center of the sphere with a cloud of electrons (bound and free) around it. The Average Atom Model is based on the Hartree-Fock-Slater (HFS) model, which solves the one-electron Schrodinger equation $\left[-\frac{1}{2}\Delta + W(\vec{r})\right]\psi_\alpha(\vec{r}) = \varepsilon\psi_\alpha(\vec{r})$ for each atomic orbital with effective potential energy $W(r)$ that includes the Coulomb potential of electrons and ion, as well as an exchange potential in the local density approximation. In practice, the wave functions are decomposed in a

spherical basis according to $\psi_\alpha(\vec{r}) = \frac{u_\alpha(r)}{r} Y_{lm}(\theta,\varphi)$, where Y_{lm} is a spherical harmonic, n is the principal and l is the orbital quantum number, and the radial part of the wave function u_α is calculated from the spherically symmetric radial Schrodinger equation (atomic units used in this section)

$$\left[-\frac{1}{2}\frac{d^2}{dr^2} + \frac{\ell(\ell+1)}{2r^2} + W(r)\right] u_\alpha(r) = \varepsilon_\alpha u_\alpha(r) \tag{7}$$

for both bound ($\varepsilon_\alpha < 0$), $\alpha = \{n\ell\}$ and continuum states ($\varepsilon_\alpha > 0$), $\alpha = \{\varepsilon\ell\}$. For bound states, the radial part of the wave function satisfies boundary conditions $u_\alpha(r) = 0$ at $r = 0$ and $\frac{d}{dr}\left(\frac{u_\alpha(r)}{r}\right) = 0$ at $r = r_{WS}$ and is normalized according to $\int_0^{r_{WS}} u_\alpha^2(r) = 1$ [29]. For scattering states, the well-known scaling at the origin, $u_\alpha \sim r^{\ell+1}$, is used to compute the first two values of the radial wave function in order to start the outward integration. The wave function is normalized by matching it to the analytical solution outside the Wigner-Seitz radius, $u_{\varepsilon,\ell}(r) = \sqrt{\frac{2k}{\pi}} r\left[j_\ell(kr)\cos(\delta_{\varepsilon,\ell}) - n_\ell(kr)\sin(\delta_{\varepsilon,\ell})\right]$, where the potential energy is zero. Here, j_ℓ and n_ℓ denote the spherical Bessel functions of first and second kind, $k = \sqrt{2\varepsilon}$ is the wave vector and $\delta_{\varepsilon,\ell}$ is the phase shift [29]. The electron density is calculated from the wave functions:

$$n_e(r) = \frac{1}{4\pi r^2}\left[\sum_{n,\ell} 2(2\ell+1) f(\varepsilon_{n\ell}) u_{n\ell}^2(r) + \sum_\ell 2(2\ell+1)\int_0^\infty f(\varepsilon) u_{\varepsilon,\ell}^2(r) d\varepsilon\right] \tag{8}$$

and then used to determine the potential energy entering Equation (7):

$$W(r) = -\frac{Z}{r} + \int_0^{r_{WS}} \frac{n_e(r')d^3r'}{|\vec{r} - \vec{r}'|} - \left(\frac{3n_e(r)}{\pi}\right)^{1/3}, \tag{9}$$

where function $f(\varepsilon) = \frac{1}{1 + \exp[(\varepsilon - \mu)/T_e]}$ is the Fermi statistical occupancy for electrons with kinetic energy ε. The first two terms in Formula (9) comprise the Coulomb potential energy (electron-nucleus and electron-electron), while the last one is the exchange term in the limit $T_e \to 0$. For finite temperatures, it is divided by a factor $1 + 3T_e/(2\varepsilon_F)$, as suggested by Murillo *et. al.* [30]. The combined formula reproduces the limiting cases of zero and high electron temperatures derived by Gupta and Rajgopal [39]. Equations (7-9) are closed by the quasi-neutrality condition $Z = \int_0^{r_{ws}} 4\pi r^2 n_e(r,\mu) dr$, which is used to derive the chemical potential μ. The average ion charge, $\bar{Z}$, is defined as the number of free electrons, which is an integral of the second term in Eq. (8). The input parameters in the Average Atom Model are the atomic number Z, electron temperature T_e, and ion density n_i. The model adopted is of the simplest kind and more advanced versions exist that will be discussed in Section 4.

The collisional and transport coefficients are calculated from the electron-ion momentum transfer cross section $\sigma_{mom}(\varepsilon) = \frac{4\pi}{k^2}\sum_{\ell=0}^{\infty}(\ell+1)\sin^2(\delta_{\ell+1} - \delta_\ell)$, which is computed from the phase shifts δ_ℓ. The electron-ion collision rate $\nu_{ei}(T_e) = \langle \sigma_{mom}(\varepsilon) \mathrm{v}(\varepsilon) \rangle n_i$ is calculated by averaging the momentum transfer cross section over the Fermi-Dirac distribution $f(\varepsilon)$ and density of states of free electrons $g(\varepsilon)$, the latter also being computed from the Average Atom Model. The *dc* electrical and thermal conductivities are $\sigma_{dc} = K_0$ and $\kappa_{dc} = \frac{K_2 - K_1^2/K_0}{T_e}$, respectively, where

$K_n = -\frac{1}{3}\int_0^\infty \tau_c(\varepsilon) v_e^2(\varepsilon) \varepsilon^n g(\varepsilon) \frac{\partial f(\varepsilon)}{\partial \varepsilon} d\varepsilon$ with $\tau_c(\varepsilon) = \left(\sigma_{mom}(\varepsilon) v(\varepsilon) n_i\right)^{-1}$ being the energy-dependent collision time [40,41]. The electron heat capacity, $C_e(T_e) = \partial U(T_e)/\partial T_e$, follows directly from the internal energy $U(T_e) = \int_0^\infty \varepsilon g(\varepsilon) f(\varepsilon, T_e) d\varepsilon$ and the electron-ion coupling constant takes the conventional form $G(T_e) = \frac{3m_e}{M_i} \nu_{ei}(T_e) n_e(T_e) k_B$.

The Average Atom Model used in this work has been extensively benchmarked. Sample results are plotted in Figure 3 for the average ion charge, chemical potential, electrical and thermal conductivities of Al, and compared to data published in the literature [16,28,30,42,43,44,45]. For T_e << 10 eV the Average Atom Model predicts $\bar{Z} \cong 3$, in agreement with the fact that in Al at solid density and room temperature 3 electrons out of 13 are free and reside in the conduction band. The chemical potential μ is also well reproduced. The model prediction for the electrical conductivity is flat for $T_e < 3$ eV, in contrast to more advanced models such as neutral-pseudoatom approach and QMD, but still reasonably well reproduced by the Average Atom Model. The thermal conductivity increases with T_e, in agreement with other calculations.

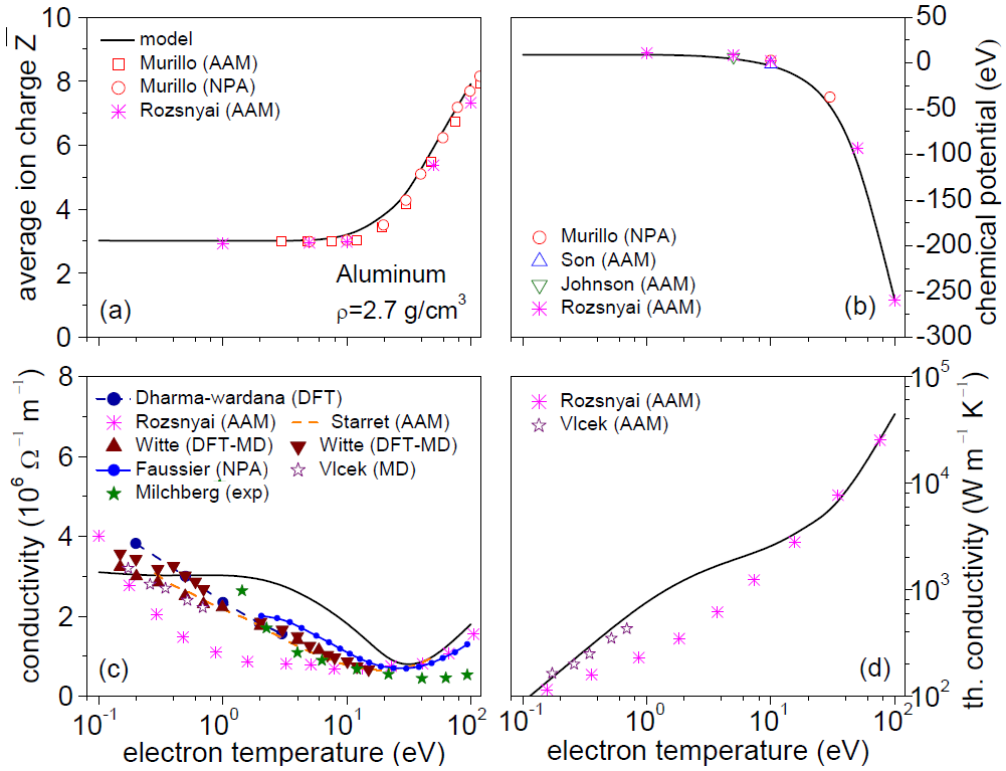

Figure 3: Average ion charge (a), chemical potential (b), electrical (c) and thermal conductivity (d) for Al calculated by the Average Atom Model (solid lines) and compared to other published data.

The collisional and transport parameters for Al in the solid and plasma states are plotted versus electron temperature in Figure 4. The data in the plasma state are calculated with the Averaged Atom Model developed in the work. The data in the solid state are calculated using formulas (2)-(5). Only the electron-ion coupling constant, plotted in Figure 4a, has been taken from the literature (Refs. [24,46]). Unfortunately, in the solid state it is available only for electron temperature $T_e < 2$ eV. In the plasma state, it has been computed in the entire temperature range of interest. For $T_e < 10$ eV G is constant, but for higher temperatures it increases, i.e. more energy is transferred from electrons to ions. The increase is primarily due to the increase of the average ion charge $\bar{Z}$ (Figure 3a) and electron density $n_e = \bar{Z} n_i$. In Figure 4b, the normalized electron heat capacity, $\bar{C}_e$, is plotted in the solid and plasma states. For both, it follows the same trend and is nearly equal in both states (solid and plasma). It increases linearly

with T_e, following the well-known scaling of strongly degenerate plasma, $\bar{C}_e(T_e) = \frac{\pi^2 k_B T_e}{2\varepsilon_F}$ (Eq. 4 in the limit $T_e \ll \varepsilon_F$), and gradually transitions to the limiting case of ideal gas, i.e. $\bar{C}_e \to 3/2$. The electron-phonon collision rate is plotted in Figure 4c for lattice temperature 300 K. In the solid state, it is constant according to Equation (2) (only lattice temperature dependence). In the plasma state, increases with T_e for the same reason the electron-phonon rate increases. For very large electron temperatures (~40-50 eV), it gradually transitions into the classical (Spitzer's) rate and starts to decrease. The electron-electron collision rate is common for both the solid and plasma states (Figure 4d). The electrical and thermal conductivities are plotted in Figures 4e and 4f, respectively. The electrical conductivity in the solid state, calculated by the Drude model (Equation 5a), differs markedly from that in the plasma state. The thermal conductivity follows a similar trend (fast increase with T_e) being larger in the solid state.

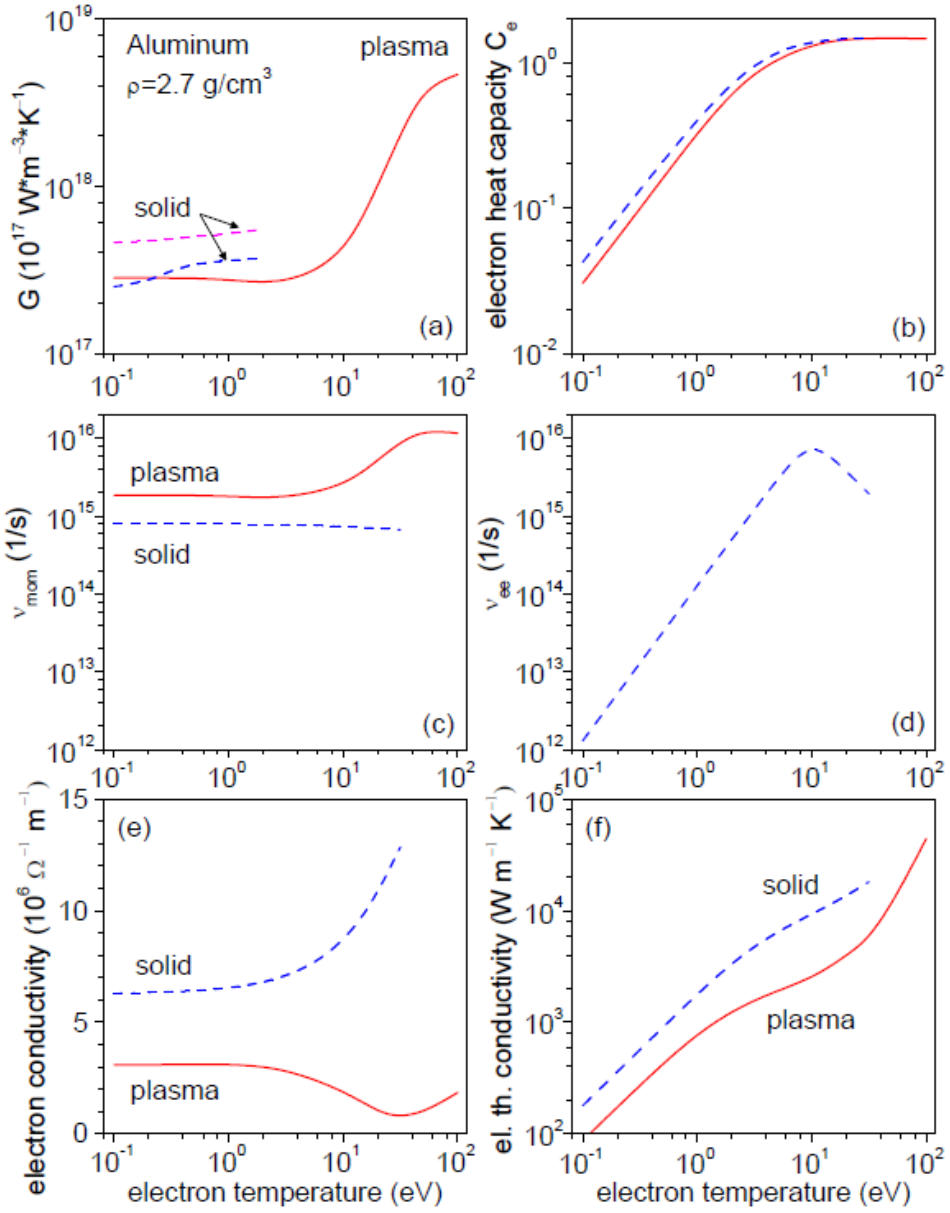

Figure 4: Electron-ion coupling constant (a), normalized electron heat capacity (b), electron-ion momentum-transfer collision rate (c), electron-electron collision rate (d), electrical conductivity (e) and thermal conductivity (f) for Al calculated by the Average Atom Model in the plasma state (solid lines) and solid state (dashed lines).

For convenience, a fit of the parameters in the plasma state is listed below, valid for $T_e < 50$ eV.

$$\bar{Z}(T_e) = \frac{3+2.5\times10^{-3}T_e^2}{1+2.5\times10^{-4}T_e^2} \tag{10a}$$

$$\bar{C}_e(T_e) = \frac{3}{2}\frac{T_e}{\sqrt{22+T_e^2}} \tag{10b}$$

$$\nu_{mom}(T_e) = 2\times10^{15}\,\frac{1+4\times10^{-3}T_e^2}{1+5\times10^{-5}T_e^{5/2}}\ (\mathrm{s}^{-1}) \tag{10c}$$

$$\sigma_{dc}(T_e) = 3\times10^{6}\,\frac{1+4\times10^{-5}T_e^3}{1+3\times10^{-3}T_e^2}\ (\Omega^{-1}\mathrm{m}^{-1}) \tag{10d}$$

$$k_e(T_e) = 1\times10^{3}\,\frac{1+1.5\times10^{-3}T_e^2}{1+0.35T_e}\ (\mathrm{Wm}^{-1}\,\mathrm{K}^{-1}) \tag{10e}$$

$$G(T_e) = 4.6\times10^{17}\left(1+0.1\sqrt{T_e}\right)\ (\mathrm{Wm}^{-3}\,\mathrm{K}^{-1}) \tag{10f}$$

Overall, the differences between the individual parameters in the solid and plasma states are within a factor or two or less (except for the electrical conductivity). A smooth interpolation between them is given by the following formula:

$$X = e^{-(T_e/T_m)^2}X^{solid} + \left(1-e^{-(T_e/T_m)^2}\right)X^{plasma}, \tag{11}$$

in which the transition point is the melting temperature of the metal. However, the interpolation proposed in this work differs from the conventional one [2,9] as depicted in Figure 5. The former interpolates between values for a fixed electron temperature, while the latter interpolates between values from temperature regimes that are far apart (below 1-2 eV and above 50-60 eV). In the conventional scheme most of the simulations are done are in the poorly defined interpolation region between ~2 and ~50 eV, while in our scheme the interpolation is between phase transitions that last a few fs only.

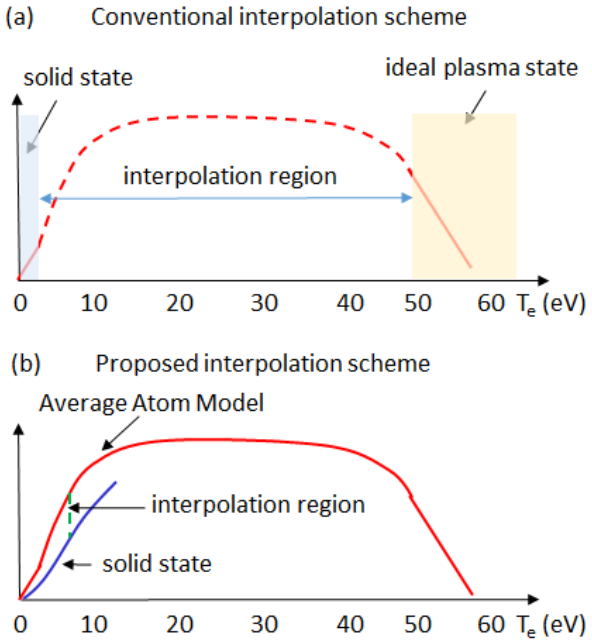

Figure 5: Conventional interpolation scheme (a) and interpolation scheme used in this work (b). The conventional scheme bridges a wide temperature gap, while the one proposed in this work interpolates between values for the same temperature.

It should be noted that the melting temperature, T_m, is a function of density. In Cowan's QEOS model, which is widely used in practice, the density dependence of the melting temperature relates to the Debye temperature, Θ_D, via the Lindmann melting law $\frac{T_m(\rho)}{\Theta_D(\rho)} = \alpha/\rho^{\frac{2}{3}}$ [47]. In this work, we consider no density variation and T_m is a fixed number. However, in hydro simulations with density variation, e.g. ablation, the melting temperature must be adjusted accordingly.

3. Simulation results.

In this section, numerical simulations for Al at solid density will be presented with emphasis on melting of the interior of the metal. This is of particular interest to us since it separates the solid from liquid phase and, more importantly, in our model it delineates the switch from solid to plasma in the Warm Dense Matter regime. Upon melting, the collisional and transport parameters in Equation (1) must transition accordingly with the interpolation given by Formula (11). The target is assumed to be infinitely long with the surface located at z=0, and infinitely wide. For both electrons and ions, Equations (1) are solved with boundary conditions $\frac{dT(t,z=0)}{dz}=0$ and $T(t,z=L)=0$, where L is the length of the computational domain, typically L=2 μm, and initial conditions $T(t=0,z)=300\,K$. Energy losses due to black body radiation from the surface have been neglected. Justification is provided in the next paragraph. The laser pulse temporal intensity profile is of the form $I(t)=AI_0\sin^2\left(\frac{\pi t}{2\tau}\right)$ having peak intensity I_0 and duration τ full width of half maximum (FWHM) (2τ at the base). The laser fluence is $F=\int_0^\infty I(t)dt=I_0\tau$. A key laser-target interaction parameter is the absorption coefficient of the metal surface, A. While in some works it is calculated dynamically (as a function of time) from the Maxwell equations using the Drude theory [8,9,11], we opted for a safer and more reliable approach. We use time-average (over the whole laser pulse) absorption coefficient, which depends only on the laser fluence: $A(F)=0.13\left(1+3.2\times10^{-5}F^{1/2}\right)$ [8,48] with the laser fluence in units of J/m^2. The choice has been motivated, in part, by the fact that experimental measurements are usually time averaged and provide a single number for a given laser fluence. The coefficients for electron-phonon and electron-electron collision frequencies are k_s=18.8 and k_e=1, respectively [19]. The thermodynamic data for Al are listed in Table 1. The normalized parameters in Equation (1) are $\Delta\bar{H}_m\cong1.29\times10^3\,K^{-1}$ and $\bar{C}_i=C_i/R\cong2.9$.

Table 1: Thermodynamic data for Al used in the two-temperature model. The data are from https://en.wikipedia.org/wiki/Aluminium.

parameter	**variable**	**value**
density	ρ	2700 kg/m^3
melting temperature	T_m	933 K
heat of fusion	ΔH_m	10.71 kJ/mol
thermal conductivity	k_i	237 W/(m*K)
molar heat capacity	C_i	24.2 J/(mol*K)

The electron and ion temperatures inside the metal are plotted in Figure 6 for laser fluence 10^4 J/m^2 (1 J/cm^2). On the left, the simulation results are for a "short" pulse with peak laser intensity I_0=10^{17} W/m^2 and pulse duration τ=0.1 ps, while on the right the results are for a "long" pulse with peak laser intensity I_0=10^{16} W/m^2 and pulse duration τ=1 ps. In all figures time t=0 refers to the time when the front of the laser pulse reaches the target surface. The first line plots simulation results for time t=0.2 ps, at the end of the "short" laser pulse. The electron temperature reaches its maximum of ~4 eV. The lattice temperature is just above the melting temperature, i.e. this is the moment the surface starts to transition from solid to liquid. At later times, t=2 ps, the lattice/ion temperature near the surface is well above the melting temperature and nearly half the electron temperature. At later times, the electron and ion temperatures equilibrate. In addition, thermal diffusion causes both temperatures to gradually penetrate the interior of the metal to a distance of about 1 μm. There is an additional energy loss from the metal surface due to black body radiation, but it is negligible: only 0.11 J/m^2, which is <0.01 % of the absorbed laser energy.

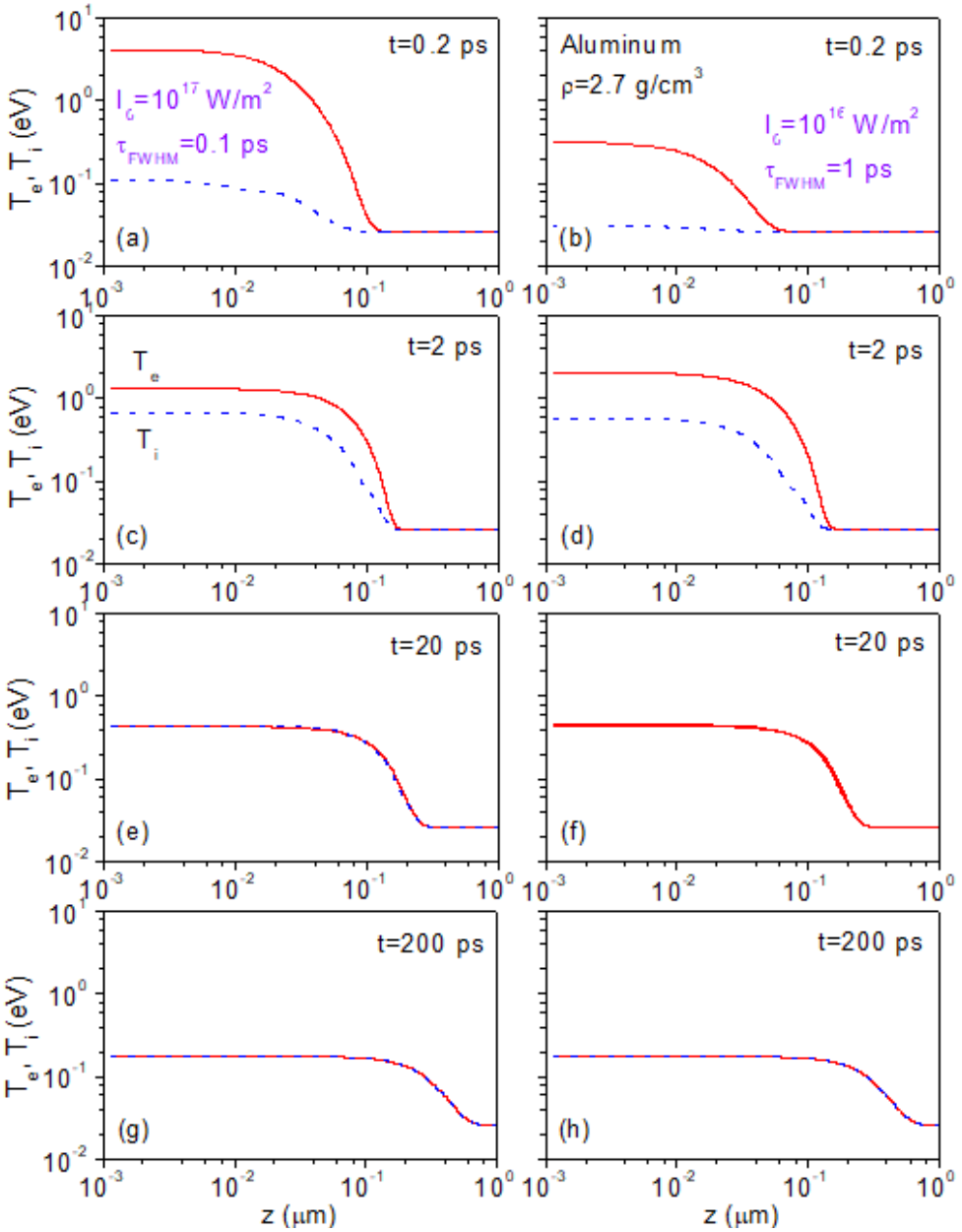

Figure 6: Electron and ion temperatures as a function of spatial position for times 0.2 ps (a,b), 2 ps (c,d), 20 ps (e,f) and 200 ps (g,h). Left: peak laser intensity 10^{17} W/m^2, pulse duration τ=0.1 ps. Right: peak laser intensity 10^{16} W/m^2, pulse duration τ=1 ps. The laser fluence is 10^4 J/m^2 for both cases.

The temperatures on the metal surface are critical for phenomena such as thermionic emission and ablation. Figure 7 plots the temporal evolution of the surface electron and ion temperatures for various laser fluences. The pulse duration is set to τ=0.1 ps. Equilibration occurs on a picosecond time scale, between 1.5 and 5 ps depending on the laser fluence (left panels). The surface reaches melting temperature in about 0.2 ps. During melting, the lattice/ion temperature flattens for about ~0.1 ps since during the solid-to-liquid phase transition energy is absorbed (the latent heat of formation), but the temperature stays constant (equal to the melting temperature). After equilibration, the surface temperatures gradually decrease with a time constant of 0.5-1 ns (right panels). It takes between one and several nanoseconds for the surface to cool off, which may have implications for processes such as thermionic emission of electrons.

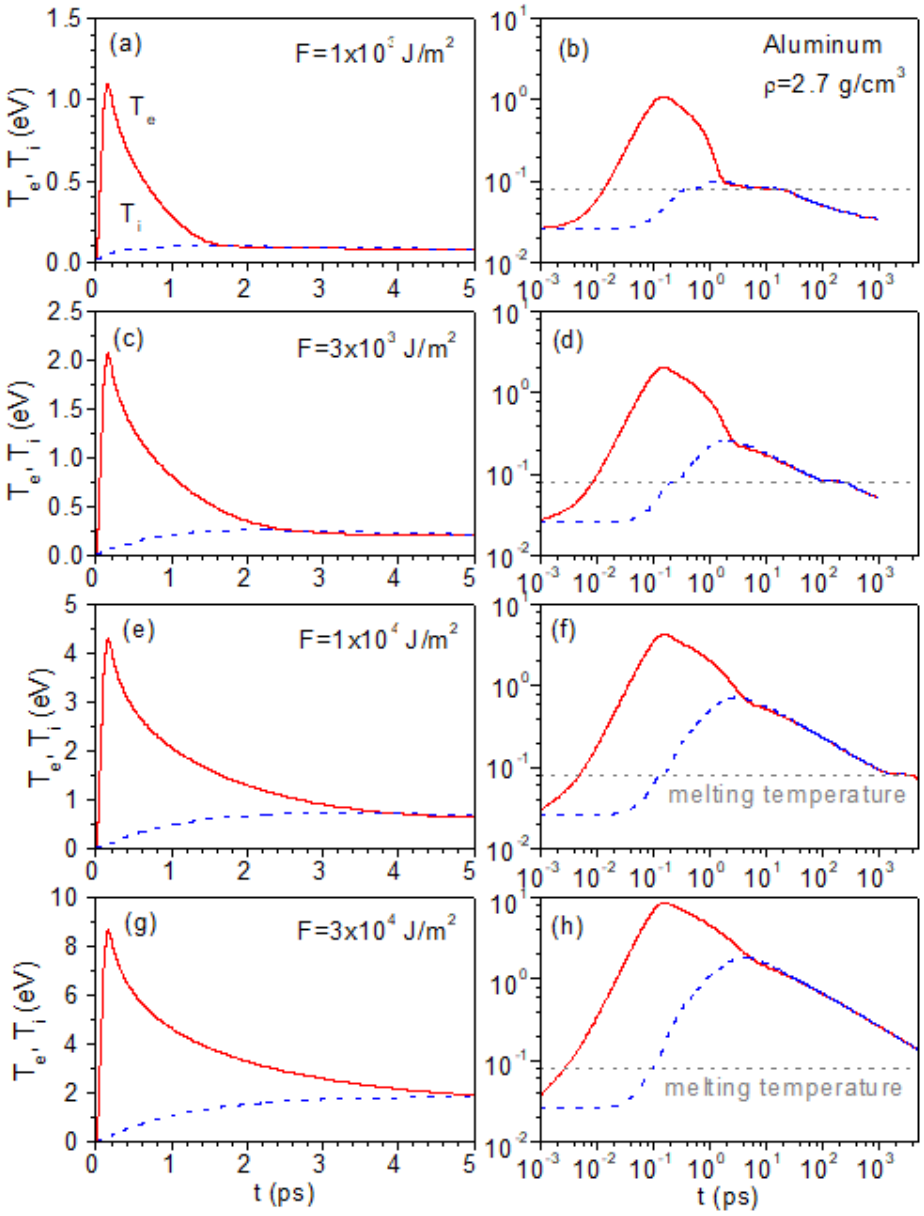

Figure 7: Electron and ion temperatures on the surface of the metal as a function of time for laser fluences 10^3 J/m^2 (a,b), 3×10^3 J/m^2 (c,d), 10^4 J/m^2 (e,f), and 3×10^4 J/m^2 (g,h). The pulse duration is τ=0.1 ps for all cases. The melting temperature is plotted with a gray dashed horizontal line.

As stated at the beginning of this section, melting of the metal interior is of primary interest to this study. The energy, which is deposited in a skin layer of roughly 20-30 nm, spreads inwards due to thermal diffusion. In Figure 8, we track the progress of this inward energy transfer by looking at the "melting line", i.e. the position z where the lattice temperature reaches the melting temperature. This is denoted as "melting depth". As discussed in Figure 6, for laser fluence 10^4 J/m^2 at time t=0.2 ps surface melting has already commenced. Following the line in Figure 8 for that fluence (second line from top), we see that at that time the metal has melted to a depth of ~20 nm. With time the melting rapidly progresses inward and at t=0.5 ns it levels off at depth of ~350 nm. This is the maximum melt depth for that laser fluence. The pattern is similar for all laser fluences under consideration. As expected, at lower laser fluence saturation is reached faster since there is less energy (per unit area) to spread, and the melt depth is smaller. For the lowest laser fluence of 10^3 J/m^2 it is only ~35 nm, barely larger than the skin depth. In contrast, for laser fluence 3×10^4 J/m^2 the heat wave keeps going inward for ~3 ns to a melt depth of 1.5 μm.

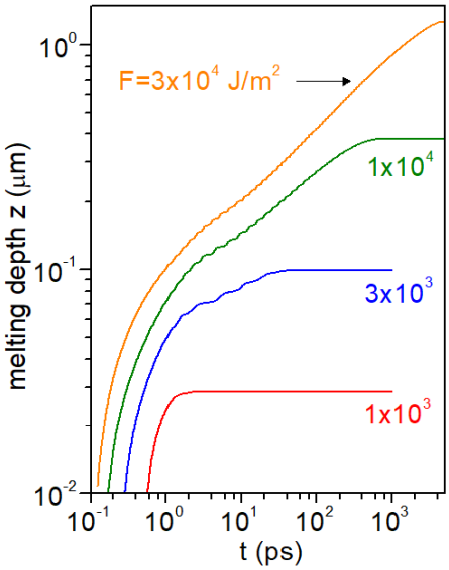

Figure 8: Melting depth of Al versus time for various laser fluences. The pulse duration is τ=0.1 ps.

The results are summarized in Figure 9, where we plot the melting depth versus laser fluence. For reference we plot the peak surface electron and lattice/ion temperatures (Figure 9, left panel). The data are taken at the end of the laser pulse. The lattice/ion temperature increases linearly with laser fluence. The electron temperature increases sub-linearly due to two factors: the electron heat capacity, which is a function of T_e, and the thermal conduction, a strong function of T_e itself, which conducts more heat at higher electron temperature thus reducing the electron temperature on the surface. The melting depth increases linearly with laser fluence. This relationship can become important in a more practical sense being relevant to the so-called heat affected zone [49,50] that affects the chemical and material composition and has implications in material processing. The melting depth, however, should not be identified as ablation depth.

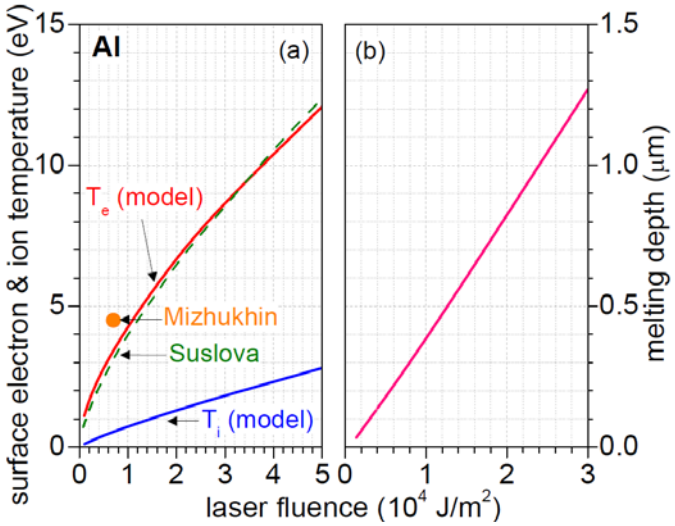

Figure 9: Electron and ion temperatures on the surface of the metal (a) and melting depth (b) as a function of laser fluence. The pulse duration τ=0.1 ps.

Since the main purpose of the proposed methodology is to use rigorously computed data, we benchmarked our simulation results with published data. Figure 9a compares the computed maximum electron temperature on the metal surface with other sources [8,51]. Both the magnitude and trend of the electron temperature with laser fluence are in agreement with other sources.

4. Discussion.

The collisional and transport parameters of the two-temperature model have been calculated

rigorously using a quantum-based model. In this work, we implemented the basic version of the Average Atom Model, which is straightforward and not difficult to develop, but is sufficient to convey the main point of the paper. In this section, we will discuss possible extensions and improvements. Ever since its first practical implementation by Liberman [27], the Average Atom Model underwent numerous improvements. Some of them are only marginally relevant to this work, for example relativistic corrections [28,29]. Starrett *et. al* took the Average Atom Model to the next level by accounting for both the electronic and ionic structures of plasma. In particular, ion correlation effects have been included that take into account the penetration of adjacent ions into the ion sphere under consideration [52]. Thiele *et. al* included the effect of screening on the atomic orbitals; work that includes subtle effects, but is more relevant to the bound states [53]. Some of the improvements, directly relevant to our work, is the inclusion of the ion structure factor $S(k)$ into the electron-ion momentum transfer cross section [32, 54]. It can be incorporated particularly easy into the basic version of the Average Atom Model, when adjacent ions do not penetrate into the Wigner-Setz sphere, since an analytical form of $S(k)$ exists [54]. The procedure for computing the momentum transfer cross section is only marginally more complicated since it involves the computation and integration of the differential cross section rather than integrated cross section directly. On the theoretical side, more rigorous derivation and use of the Average Atom Model based on the variational principle was proposed by Piron and Blenski [55]

The Average Atom Model has undergone development in another direction, pioneered by Dharma-wardana and Perot in the early 90's [56,57]. They developed the so-called neutral-pseudoatom Approach (NPA) [30,44,58,59,60], which overcomes many of the limitations of the original Average Atom Model. In particular, the electron wave-functions are no longer confined to the Wigner-Seitz sphere, but allowed to extend far beyond its boundary in a natural way into a correlation sphere with radius $\sim 10 r_{ws}$. The accuracy is improved albeit at the cost of complexity and computation time. The latter is still reasonable (minutes/run) and can be used for mass-production of collisional data.

Finally, it is worth noting that other options for generation of complete data sets exist. A notable example is Ref. [11], in which an analogous set of data for Cu was produced by the FP-LMTO model. But the Average Atom Model has several unique features that makes it highly desirable. In addition to being fully quantum, it has the virtues of conceptual simplicity and straightforward numerical development. Speed, robustness and versatility make it the method of choice when large data sets are required in problems such as ablation. Last, but not least, the Average Atom Model can be applied to a variety of metals, e.g. Na, Be, Fe, Cu, and Au.

The second discussion point is the data implementation. We restricted ourselves to a relatively straightforward application for constant ion density, but the consequences are far-reaching. More advanced models of laser ablation based on hydro simulations can benefit from the proposed approach too, except a data table should be made in the density-temperature configuration space rather than temperature dependent only as it was done in this work. Since the Average Atom Model is extremely fast and it can cover smoothly the density-temperature domain in a very wide range of conditions, appropriate tables for each parameter can be easily generated, including Equation of State (EoS), pressure as a function of density and temperature [61]. Thus, the applicability of the proposed approach can be extended far beyond what was demonstrated here to tackle more complex problems.

5. Conclusions

Analytical formulas for collisional and transport parameters of Al in the *solid state* are combined with data calculated from the Average Atom Model for the *plasma state* to produce a complete set for modeling laser-metal interactions at moderate intensities (10^3-10^5 J/m^2). The separation between solid and plasma states is based on the *physical condition* of the lattice with a uniquely defined transition point, which is in contrast to other models that use the electron temperature as a demarcation line. Another critical difference is the use of a fully quantum model suitable for plasmas in the Warm Dense Matter regime instead of Spitzer-like models adopted in previous works. Thus, the accuracy of power deposition rate, collisional and transport parameters has been improved.

The data were incorporated into a two-temperature model and applied to the important case of

lattice melting. Surface heating and melting depth have been calculated as a function of temperature for laser fluences varying from 10^3 J/m^2 to 3×10^4 J/m^2. It was found that the melting depth increases linearly with laser fluence.

The approach proposed in this work can be extended to more complex situations such as laser ablation that involve hydrodynamic motion of the plasma.

Acknowledgements
This work was supported by the NRL Base Program. This research was performed while A.D. held an NRC Research Associateship award at NRL.

References:

1 S. Nolte, C. Momma, H. Jacobs, A. Tunnermann, B. N. Chichkov, B. Wellegehausen, and H. Welling, J. Opt. Soc. Am. B **14**, 2716-2722 (1997)
2 B. Chimier, V. T. Tikhonchuk, and L. Hallo, Phys. Rev. B **75**, 195124 (2007)
3 X. Zhao and Y. C. Shin, Applied Surface Science **283**, 94-99 (2013)
4 C. W. Cheng, S. Y. Wang, K. P. Chang, and J. K. Chen, Applied Surface Science **361**, 41-48 (2016)
5 T. Balasubramani and S. H. Jeong, Journal of Physics: Conference Series **59**, 595–599 (2007)
6 T. Wang, J. Guo, J. Shao, D. Wang, A. Chen, and M. Jin, Phys. Plasmas **22**, 033106 (2015)
7 G. M. Petrov, J. P. Palastro, and J. Peñano, Phys. Rev. E **95**, 053209 (2017)
8 A. Suslova and A. Hassanein, Laser and Part. Beams **35**, 415-428 (2017)
9 S. E. Kirkwood, Y. Y. Tsui, R. Fedosejevs, A. V. Brantov, and V. Yu. Bychenkov, Phys. Rev. B **79**, 144120 (2009)
10 L. Jiang and H.-L. Tsai, J. Appl. Phys. **104**, 093101 (2008)
11 P. A. Loboda, N. A. Smirnov, A. A. Shadrin, and N. G. Karlykhanov, High Energy Density Physics **7**, 361-370 (2011)
12 J. K. Chen, D. Y. Tzou, and J. E. Beraun, Int. J. Heat and Mass Transfer **49**, 307-316 (2006)
13 N. M. Bulgakova, R. Stojan, A. Rosenfeld, I. V. Hertel, W. Marine, and E. E. B. Campbell, Appl. Phys. A **81**, 345-356 (2005)
14 E. G. Gamaly, A. V. Rode, B. Luther-Davies, and V. T. Tikhonchuk, Phys. Plasmas **9**, 949 (2002)
15 E. G. Gamaly, S. Juodkazis, K. Nishimura, H. Misawa, B. Luther-Davies, L. Hallo, P. Nicolai, and V. T. Tikhonchuk, Phys. Rev. B **73**, 214101 (2006)
16 C. E. Starrett, Phys. Plasmas **25**, 092707 (2018)
17 K. L. Jensen, D. W. Feldman, N. A. Moody, and P. G. O'Shea, J. Appl. Phys. **99**, 124905 (2006)
18 N. A. Papadogiannis, S. D. Moustaïzis, and J. P. Girardeau-Montaut, J. Phys. D **30**, 2389-2396 (1997)
19 K. Eidmann, J. Meyer-ter-Vehn, T. Schlegel, and S. Huller, Phys. Rev. E **62**, 1202-1214 (2000)
20 C. Kittel, "*Introduction to Solid State Physics*", John Wiley & Sons, Inc., 8-th Edition (1986)
21 N. W. Ashkroft and N. D. Mermin, "*Solid State Physics*", Saunders College Publishing (1976)
22 B. Y. Mueller and B. Rethfeld, Phys. Rev. **87**, 035139 (2013)
23 A. V. Lugovskoy and I. Bray, Phys. Rev. B **60**,3279 (1999)
24 Z. Lin, L. V. Zhigilei, and V. Celli, Phys. Rev. **77**, 075133 (2008)
25 J. Simoni and J. Daligault, Phys. Rev. Lett. **122**, 205001 (2019)
26 F. F. Chen, Phys. Plasmas **8**, 3008-3017 (2001)
27 D. A. Liberman, Phys. Rev. B **20**, 4981-4989 (1979)
28 B. F. Rozsnyai, Phys. Rev. A **5**, 1137-1149 (1972)
29 T. Blenski and K. Ishikawa, Phys. Rev. E **51**, 4869-4881 (1995)
30 M. S. Murillo, J. Weisheit, S. B. Hansen, and M. W. C. Dharma-wardana, Phys. Rev. E **87**, 063113 (2013)
31 W. R. Johnson, C. Guet, and G. F. Bertsch, JQSRT **99**, 327-340 (2006)
32 J. C. Pain and G. Dejonghe, Contrib. Plasma Phys. **50**, 39-45 (2010)

33 W. R. Johnson, High Energy Density Physics **5**, 61-67 (2009)
34 C. E. Starrett, J. Clérouin, V. Recoules, J. D. Kress, L. A. Collins, and D. E. Hanson, Phys. Plasmas **19**, 102709 (2012)
35 C. E. Starrett, N. M. Gill, T. Sjostrom, and C. W. Greeff, Computer Phys. Comm. **235**, 50-62 (2019)
36 S.-K. Son, R. Thiele, Z. Jurek, B. Ziaja, and R. Santra, Phys. Rev. X **4**, 031004 (2014)
37 E. Wigner and F. Seitz, Phys. Rev. **43**, 804-810 (1933)
38 E. Wigner and F. Seitz, Phys. Rev. **46**, 509-524 (1934)
39 U. Gupta and A. K. Rajagopal, Phys. Rev. A **21**, 2064-2068 (1980)
40 T. Lee and R. M. More, Phys. Fluids **27**, 1273-1286 (1984)
41 D. J. Burrill, D. V. Feinblum, M. R. J. Charest, and C. E. Starrett, High Energy Density Physics **19**, 1-10 (2016)
42 V. Vlcek, N. de Koker, and G. Steinle-Neumann, Phys. Rev. B **85**, 184201 (2012)
43 G. Faussurier and C. Blancard, Phys. Rev. E **91**, 013105 (2015)
44 M. W. C. Dharma-wardana, D. D. Klug, L. Harbour and L. J. Lewis, Phys. Rev. E **96**, 053206 (2017)
45 B. B. L. Witte, G. Röpke, P. Neumayer, M. French, P. Sperling, V. Recoules, S. H. Glenzer, and R. Redmer, Phys. Rev. E **99**, 047201 (2019)
46 J. Simoni and J. Daligault, Phys. Rev. Lett. **122**, 205001 (2019)
47 R. M. More, K. H. Warren, D. A. Young, and G. B. Zimmerman, Physics of Fluids **31**, 3059 (1988)
48 A. M. Komashko, M. D. Feit, A. M. Rubenchik, M. D. Perry, and P. S. Banks, Appl. Phys. A **69** [Suppl.], S95–S98 (1999)
49 Y. Hirayama and M. Obara, J. Appl. Phys. **97**, 064903 (2005)
50 X. Jia and X. Zhao, Applied Surface Science **463**, 781-790 (2019)
51 A. V. Mazhukin, V. I. Mazhukin, M. M. Demin, Appl. Surface Science **257**, 5443–5446 (2011)
52 C. E. Starrett and D. Saumon, Phys. Rev. E **87**, 013104 (2013)
53 R. Thiele, S.-K. Son, B. Ziaja, and R. Santra, Phys. Rev. A **86**, 033411 (2012)
54 B. F. Rozsnyai, High Energy Density Physics **4**, 64-72 (2008)
55 R. Piron and T. Blenski, Phys. Rev. E **83**, 026403 (2011)
56 M. W. C. Dharma-wardana and F. Perrot, Phys. Rev. A **26**, 2096-2104 (1982)
57 F. Perrot and M. W. C. Dharma-wardana, Phys. Rev. A **29**, 1378-1390 (1984)
58 L. Harbour, M. W. C. Dharma-wardana, D. D. Klug, and L. J. Lewis, Phys. Rev. E **95**, 043201 (2017)
59 C. Blancard and G. Faussurier, Phys. Rev. E **69**, 016409 (2004)
60 G. Faussurier, C. Blancard, P. Cossé, and P. Renaudin, Phys. Plasmas **17**, 052707 (2010)
61 G. Faussurier and C. Blancard, Phys. Rev. E **99**, 053201 (2019)